



Contents lists available at ScienceDirect

## Arabian Journal of Chemistry

journal homepage: [www.ksu.edu.sa](http://www.ksu.edu.sa)

# Renewal of electrical energy by green hydrogen using a metal organic framework with Fe<sub>3</sub>O<sub>4</sub> cluster

Fedaa M.M. Alrashedee, Zahraa Bakdash, Salwa Ali, Khadijah M. Emran\*

Chemistry Department, College of Science, Taibah University, Al Maddinah Al Mounwara, Saudi Arabia

## ARTICLE INFO

## Keywords:

Metal organic framework (MOF)  
Magnetite  
Electrocatalyst  
Green Hydrogen  
Lanthanides

## ABSTRACT

Recently, metal–organic frameworks (MOFs) with high porosity have drawn extensive attention in water splitting. The present study reports the synthesis of a porous Fe-based MOF by a modified precursor made of magnetite (Fe<sub>3</sub>O<sub>4</sub>). Subsequently, a series of undoped and lanthanide -doped (MOFs) are prepared using the solvothermal method. The synthesis provided a high surface area with a high specific surface and pore volume. The synthesized electrocatalyst with a high surface area is demonstrated as an excellent electrocatalyst for the hydrogen evolution reaction (HER) investigated in acidic media. The electrochemical results demonstrated low Tafel slopes (81 and 166 mV dec<sup>-1</sup>), high exchange current, high surface area (C<sub>dl</sub>) (148.29 and 150.57 mV), and high stability for Au/MIL-53 (Fe)/Gd-Fe<sub>3</sub>O<sub>4</sub> and glassy carbon electrode GCE/MIL-53 (Fe)/La-Fe<sub>3</sub>O<sub>4</sub>. The high activity is attributed to the large surface area of the synthesized Fe/ Fe<sub>3</sub>O<sub>4</sub>-based MOF, which is porous and magnetic. The effect of base metal on catalyst performance was discussed. Through the unification of two catalytically active metals as lanthanide, a new opportunity opens up for the development of synergistic systems in multiple applications.

## 1. Introduction

Global warming and air pollution are currently the main issues worldwide in the twenty-first century due to the development and usage of fossil fuels. These issues can only be handled by using alternative environmentally friendly energy sources (Qian et al., 2019); (Inderwildi et al., 2020). One of the most promising green energy sources is hydrogen (H<sub>2</sub>), which is a clean, abundant, and recyclable ideal fuel with a high purity (99.9 %) that can be readily used as a reactant for industrial processes (Farinotti et al., 2019); (Yalew et al., 2020); (Nie et al., 2016); (Chi and Yu, 2018). Hydrogen energy and its applications in hydrogen fuel cells are among the most eco-friendly energy options available (Abdalla et al., 2018); (Nie et al., 2020).

Green hydrogen is produced from renewable water and electricity through the electrolysis process which splits water into hydrogen (H<sub>2</sub>) and oxygen (O<sub>2</sub>) while being powered by electricity with zero carbon emissions. Hydrogen has a significantly higher energy density than gasoline, at 120 MJ kg<sup>-1</sup>, as compared to 44 MJ kg<sup>-1</sup> for gasoline. Additionally hydrogen fuel cells have an energy density that is up to four

times than that batteries (Carmo et al., 2013); (Amiinu et al., 2017); (Zhou et al., 2018); (Amiinu et al., 2018); (Lu et al., 2019). Another crucial half-reaction that occurs during water electrolysis is hydrogen evolution. Pt remains to be the HER catalyst with the lowest overpotentials in use today. However, its large-scale use in water electrolysis is limited by its availability and high cost. Therefore, highly active precious-metal free catalysts for HER are therefore crucial for promoting the use of electrochemical hydrogen (Lu et al., 2019); (Wang et al., 2020); (Radwan et al., 2021); (Liang et al., 2022).

Recently, metal–organic frameworks (MOFs), constructed from well-dispersed metal/cluster nodes periodically coordinated with organic linkers of a tunable porous structure and defined crystal structure, have been considered as potential catalysts for hydrogen production from water splitting. Their flexible structure, ultra-large surface area, stable porous design, and chemical component diversification make them crucial for industrial application. Additionally, MOFs contain active centers, including transition metal sites and functional groups, which can interact with other molecules. This implies that MOFs are promising molecules for sensing and catalytic applications. However, the natural

Peer review under responsibility of King Saud University.

\* Corresponding author.

E-mail addresses: [fu3f@hotmail.com](mailto:fu3f@hotmail.com) (F.M.M. Alrashedee), [Zsbakdash@gmail.com](mailto:Zsbakdash@gmail.com) (Z. Bakdash), [Ssllooa2000@gmail.com](mailto:Ssllooa2000@gmail.com) (S. Ali), [kabdalsamad@taibahu.edu.sa](mailto:kabdalsamad@taibahu.edu.sa) (K.M. Emran).

<https://doi.org/10.1016/j.arabjc.2024.105734>

Received 16 January 2024; Accepted 14 March 2024

Available online 15 March 2024

1878-5352/© 2024 The Authors. Published by Elsevier B.V. on behalf of King Saud University. This is an open access article under the CC BY-NC-ND license (<http://creativecommons.org/licenses/by-nc-nd/4.0/>).

characteristic of MOFs is low conductivity because of their organic components. Thus, MOFs are usually incorporated with high conductive materials to enhance performance in electrochemical applications (Xue et al., 2019); (Tu et al., 2021); (Cheng et al., 2021); (Do et al., 2022). Due to the large ionic radii of the lanthanides and their huge coordination numbers, rare earth elements are also used as a source of metal centers and can thus create unique MOFs structures (Ali et al., 2023); (Wu et al., 2022).

In extension, a controlled partial phosphorylation strategy was used to dope CoP species onto the surface of the Co-MOF carbon fiber paper. This process revealed unique porous structure of Co-MOF, which expose more active sites and facilitate the release of generated gas, as synthesized CoP/Co-MOF hybrid demonstrated outstanding HER performance in 1 M phosphate buffer solution, 0.5 M H<sub>2</sub>SO<sub>4</sub> and 1 M KOH media. The enhancement in HER performance is derived from the electron transfer from CoP to Co-MOF through N-P and N-Co bonds (Liu et al., 2019).

Huang et al. designed a new type of conductive MOFs with in-plane mesoporous structures (Huang et al., 2020). The MOF was made up of hexaiminohexa-azatrinaphthalene (HAHATN), which is used as a conjugated ligand to construct bimetallic sited (Ni<sub>3</sub>(Ni<sub>3</sub>•HAHATN)<sub>2</sub>) MOFs with an extra Ni—N<sub>2</sub> moiety in-plane mesoporous structure. The fully conjugated conductive MOFs M<sub>23</sub>(M<sub>13</sub>•HAHATN)<sub>2</sub> (M<sub>1</sub>:Co or Cu, M<sub>2</sub>:Ni or Cu) obtained in this study were converted to reversible hydrogen electrodes in a 1 M KOH solution. The highest electroactivity of Ni<sub>3</sub>(Ni<sub>3</sub>•HAHATN)<sub>2</sub> toward HER confirm that unsaturated M<sub>1</sub>—N<sub>2</sub> site can serve as a highly active center to address the short coming of traditional conductive MOFs in electrocatalysis. A new Fe(OH)<sub>x</sub>@Cu-MOF with 2,3,6,7,10,11-hexahydroxytriphenylene (HHTP) molecules as the organic linkers was designed (Cheng et al., 2021). The electrochemical results reveal that the local electronic polarization of unsaturated Cu<sub>1</sub>-O<sub>2</sub> centers in the Cu-MOF outer layer is essential in promoting the formation of adsorbed \*H intermediates, thus significantly enhancing the HER kinetics.

One type of MOF is known as MIL, which stands for Material of Institute Lavoisier. Ferey and his group synthesized the MIL type of MOFs for the first time in 2002 (Ali et al., 2023); (Millange et al., 2002). MIL-53 has been made from a variety of metals, such as MIL-53 (Cr), MIL-53 (Fe), and MIL-53 (Al) (Ali et al., 2023); (Millange et al., 2002); (Nguyen et al., 2019); (Liang et al., 2019). Scientists are interested in MIL-53 (Fe) because of its excellent characteristics, including minimal metal center toxicity, stability, high porosities, and flexible structure. The morphology of MIL-53 (Fe) is a dapple-cone hexagonal prism structure. Additionally, MIL-53 (Fe) exhibits great molecular flexibility since its pores only open in the presence of a guest molecule (Ali et al., 2023); (Liang et al., 2019); (Yu et al., 2020).

In the HER scope, MIL-88B MOFs templating approach to synthesize Co-incorporating FeP nanotubes (Co-Fe-P nanotubes), aiming at improving the HER catalytic performance (Chen, 2019). The good catalytic performances of Co-Fe-P nanotubes in 1 M KOH, 1 M PBS, and 0.5 M H<sub>2</sub>SO<sub>4</sub> were due to their tubular structure and tuning composition, which led to cheap and efficient FeP-based electrocatalysts for HER.

Yan et al. (Yan et al., 2017) used Ti-MOF material for (MIL)-125-NH<sub>2</sub> (Ti) synthesis, which is further loaded with palladium. The great performance of this MOF for photocatalytic HER was due to the specific surface area and Pd as a cocatalyst. The maximum was achieved with a Pd loading of 1.5 %.

Electrocatalytic property toward the HER of MIL-100(Fe) (trimesic acid, H<sub>3</sub>BTC, is organic linkers) was examined in 0.5 M H<sub>2</sub>SO<sub>4</sub> and 1.0 M NaOH (Nivetha et al., 2020). This high electrocatalytic activity of the HER in both media could be due to the high surface area with porous nature and homogeneous morphology. In the current study, we distributed La and Gd nanoparticles in MIL-53 (Fe)/Fe<sub>3</sub>O<sub>4</sub> using solvothermal synthesis and demonstrated an enhanced water-splitting hydrogen evolution reaction (HER) in acidic media. The influence of the bimetallic precursor (Fe-La) or (Fe-Gd) on the structural, surface, and thermal properties of (MIL-53 (Fe)/La-Fe<sub>3</sub>O<sub>4</sub> and MIL-53 (Fe)/Gd

-Fe<sub>3</sub>O<sub>4</sub>) will be examined. Kinetic and thermodynamic studies were conducted to determine the activation energy and the reaction mechanism.

## 2. Materials

Potassium hydroxide (KOH) (85 % Analar), iron (II) sulfate heptahydrate (FeSO<sub>4</sub>•7H<sub>2</sub>O) (99 % Sigma-Aldrich.), iron (III) nitrate nonahydrate (Fe(NO<sub>3</sub>)<sub>3</sub>•9H<sub>2</sub>O) (98 % Sigma-Aldrich.), lanthanum (III) nitrate hexahydrate (La(NO<sub>3</sub>)<sub>3</sub>•6H<sub>2</sub>O) (99 % Sigma-Aldrich.), gadolinium (III) nitrate hexahydrate (Gd(NO<sub>3</sub>)<sub>3</sub>•6H<sub>2</sub>O) (99.9 % Sigma-Aldrich.), sodium hydroxide (NaOH) (98 % Sigma-Aldrich.), terephthalic acid (C<sub>8</sub>H<sub>6</sub>O<sub>4</sub>) (98 % Sigma-Aldrich.), hydrochloric acid (HCl) (37 % Sigma-Aldrich.), ammonium hydroxide solution (NH<sub>4</sub>OH) (30–33 % Sigma-Aldrich.), nitric acid (HNO<sub>3</sub>) (69 % Sigma-Aldrich.), ethanol (C<sub>2</sub>H<sub>5</sub>O) (99.8 % Sigma-Aldrich.), N,N-Dimethyl formamide ((CH<sub>3</sub>)<sub>2</sub>NC(O)H) (DMF) (99.8 % Sigma-Aldrich.).

All reagents and solvents were used directly without further purification. The aqueous solutions in this work were prepared with high quality deionized (DI) water (18.2 MΩ cm) from a Milli-Q water purification system (Milli-Q® CLX 7000 Series, Millipore).

### 2.1. Synthesis of electrocatalytic nanoparticles

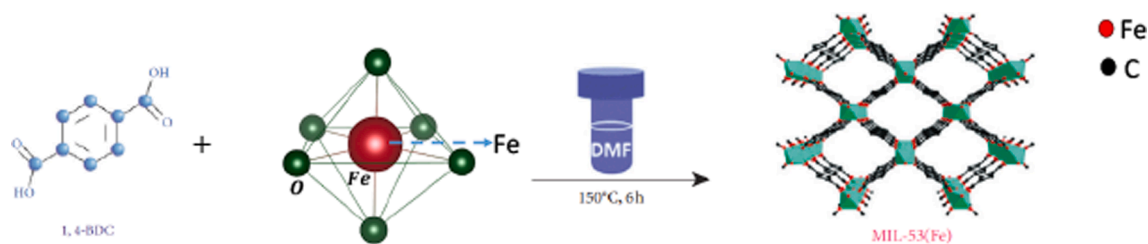
The method includes two steps. First, we synthesized magnetite nanoparticles (Fe<sub>3</sub>O<sub>4</sub>), this was achieved using the coprecipitation method as in previous studies (Ali et al., 2023); (Ali et al., 2017); (Abu-Dief et al., 2022). Briefly, in the coprecipitation method, a molar ratio of 2:1 of Fe<sup>3+</sup> and Fe<sup>2+</sup> was mixed 100 mL of deionized water under a N<sub>2</sub> atmosphere and the pH was adjusted to 10 using concentrated NaOH. The black precipitate Fe<sub>3</sub>O<sub>4</sub> nanoparticles formed and were allowed to stand for several hours. Subsequently, the precipitate was isolated by simple filtration, washed with deionized water several times and allowed to dry in a desiccator. In the case of doping a 10 % molar ratio was eliminated from the iron (III) ion and replaced by lanthanide (Gd<sup>3+</sup> or La<sup>3+</sup>) ions.

The second step was the solvothermal synthesis of MIL-53 (Fe)/Fe<sub>3</sub>O<sub>4</sub> as in previous study (Ali et al., 2023); where a molar ratio of 1:20 from magnetite nanoparticles and terephthalic acid (C<sub>6</sub>H<sub>4</sub>(CO<sub>2</sub>H)<sub>2</sub>) was mixed in 30 mL of DMF, followed by sonication for 30 min. until all TPA dissolved and the solution became homogenized. Drops of HCl were added to the homogenized mixture, placed in a 50 mL teflon-lined stainless-steel autoclave and left it in an oven at 150°C for 24 h. After cooling, the precipitate was isolated using a centrifuge, and the product was purified with several washes with ethanol, (Scheme 1) (Liu et al., 2020). For activation the product was dried at 60 °C for 6 h and a sandy brown powder was collected. The doped magnetite - MOFs of La-Fe<sub>3</sub>O<sub>4</sub> and Gd-Fe<sub>3</sub>O<sub>4</sub> were prepared and named, MIL-53 (Fe)/La-Fe<sub>3</sub>O<sub>4</sub> and MIL-53 (Fe)/Gd -Fe<sub>3</sub>O<sub>4</sub>.

### 2.2. Electrochemical cell and equipment

The electrochemical activities of different MIL materials (MIL-53 (Fe)/Fe<sub>3</sub>O<sub>4</sub>, MIL-53 (Fe)/La-Fe<sub>3</sub>O<sub>4</sub> and MIL-53 (Fe)/Gd -Fe<sub>3</sub>O<sub>4</sub>) were evaluated after being embolized on a glassy carbon electrode (GCE) or gold (Au) workstation with a typical three-electrode cell on a potentiostat/galvanostat (Gamry interface 1000 potentiostat) in 0.5 mol/L H<sub>2</sub>SO<sub>4</sub>. The working electrode was prepared by 20 μL drop cast of the catalyst on a GCE (GCE/catalyst) or Au (Au/catalyst) of 0.07 cm<sup>2</sup>. The reference electrode was Ag/AgCl with platinum wire as counter electrode (CE).

DC polarization measurements of hydrogen evolution were conducted by first stabilizing the electrode at open-circuit potential (OCP) until a steady-state OCP value was obtained (usually approximately 5 min). A cyclic voltammetry (CV) experiment was conducted at a scan rate of 100 mVs<sup>-1</sup> from 1.0 to - 0.5 V followed by linear polarization



**Scheme 1.** Schematic illustration for the preparation of MIL-53 (Fe)/Fe<sub>3</sub>O<sub>4</sub> hybrid magnetic composites.

measurement from  $-0.2$  V to  $-0.8$  V, at a scan rate of  $1 \text{ mVs}^{-1}$ . CV measurements at different sweep rates were performed in the non-Faraday voltage region to determine electrochemical double layer capacitance ( $C_{dl}$ ) by  $C_{dl} = j/\nu$ , where  $j$  is the capacitive current and  $\nu$  is a sweep rate. The DC polarization measurement was followed by a set of electrochemical impedance spectroscopy (EIS) measurements at selected overpotentials. The interfacial properties between the MIL materials / and the H<sub>2</sub>SO<sub>4</sub> interface were investigated using EIS technique with a sinusoidal voltage of 10 mV per decade and a frequency range of 100 kHz to 0.01 Hz, at a potential of  $-0.5$  V vs. reference electrode.

### 2.3. Physicochemical morphology and composition

The surface morphology and surface elemental composition of the MIL materials (MIL-53 (Fe)/Fe<sub>3</sub>O<sub>4</sub>, MIL-53 (Fe)/La-Fe<sub>3</sub>O<sub>4</sub> and MIL-53 (Fe)/Gd-Fe<sub>3</sub>O<sub>4</sub>) were investigated by scanning electron microscopy (SEM) and energy-dispersive X-ray spectroscopy (EDX) techniques using a field emission JEOL-JSM-6360 instrument. The crystalline structure of the different MOFs was analyzed by X-ray diffraction (XRD) using a Shimadzu, XRD-7000 diffractometer with a diameter of 0.5 mm. Collimated Cu K $\alpha$  ( $1.54 \text{ \AA}$ ) radiation at room temperature in a standard  $\theta$ - $2\theta$  mode. Furthermore, for chemical composition characterization, Fourier transform infrared spectroscopy (FTIR) measurements on a silicon substrate were measured using an IR Affinity-1S Spectrometer (Shimadzu, Japan). The surface area and porosity tested by nitrogen adsorption / desorption test using a Gemini VII, 2390 USA analyzer and the adsorption parameters of the samples were obtained by the Brunauer-Emmett-Teller isotherm. The thermal stability of samples was investigated by

thermogravimetric (TG) curves measured using a Q600 T (SDT Q600, TA Instruments).

## 3. Results and discussion

### 3.1. Chemical and morphological characterization

The surface structure of undoped and lanthanide-doped magnetite-based MILs was characterized by SEM. The images of MOFs in Fig. 1 (a-c) affirm several morphologies. MIL-53 (Fe)/Fe<sub>3</sub>O<sub>4</sub> and La doped MIL-53 (Fe)/La-Fe<sub>3</sub>O<sub>4</sub> in Fig. 1.a & b respectively, show a bipyramidal hexagonal prism structure shape. By contrast, MIL-53(Fe)/Gd-Fe<sub>3</sub>O<sub>4</sub> crystals in Fig. 1.c show a rod-like (calamitic) structure. The homogeneity distribution of doped ions in the samples proved clearly in EDX analysis (Abu-Dief et al., 2022) and percentage % of component from EDX analysis is shown in Fig. 1(a', b', c').

Components FTIR spectra of the MIL samples were shown in Fig. 2a, TPA coordinated with Fe<sup>3+</sup> shows in the vibrations of the C = O group at  $1600 \text{ cm}^{-1}$ . The stretching bond peak at  $1300 \text{ cm}^{-1}$  is belongs to the C-O group (Alqadami et al., 2017). The peak at  $578 \text{ cm}^{-1}$  in fingerprint region is due to the O-Fe vibration which confirms the formation of metal-oxo bond between the carboxylic group of TPA and the Fe (III) (Liu et al., 2020). Moreover, the peak at  $753 \text{ cm}^{-1}$  could be belong to the C-H bending vibration on the benzene ring and approximately  $1680 \text{ cm}^{-1}$  vibrations of C = C confirm the existence of a benzene ring in all samples (Ai et al., 2013).

The XRD pattern of prepared MIL-53 (Fe)/Fe<sub>3</sub>O<sub>4</sub> in Fig. 2b at  $2\theta = 9.174^\circ, 12.587^\circ, 18.709^\circ, 17.819^\circ, 25.369^\circ, 27.251^\circ$  and  $27.916^\circ$  was matched well with card no.: (JCPDS 220477) and data in the literature

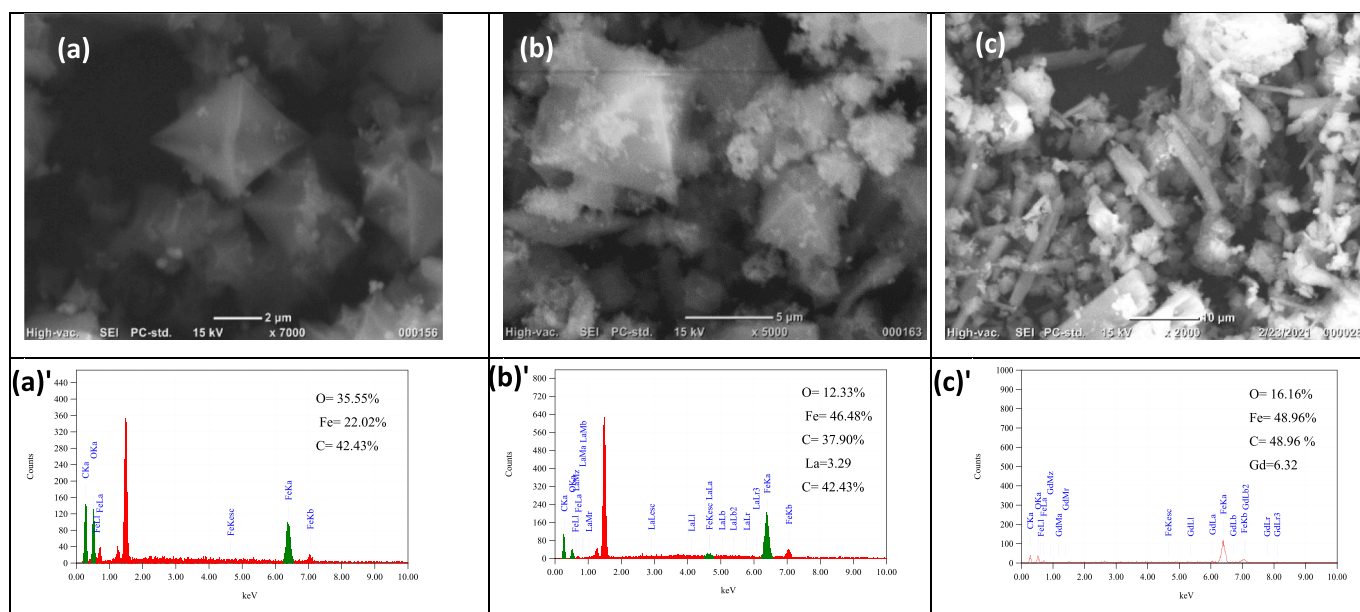


**Fig. 1.** High magnification SEM micrographs with EDX analysis of (a,a') MIL-53(Fe)/Fe<sub>3</sub>O<sub>4</sub>, (b,b') MIL-53(Fe)/La-Fe<sub>3</sub>O<sub>4</sub>, (c,c') MIL-53(Fe)/Gd-Fe<sub>3</sub>O<sub>4</sub>.

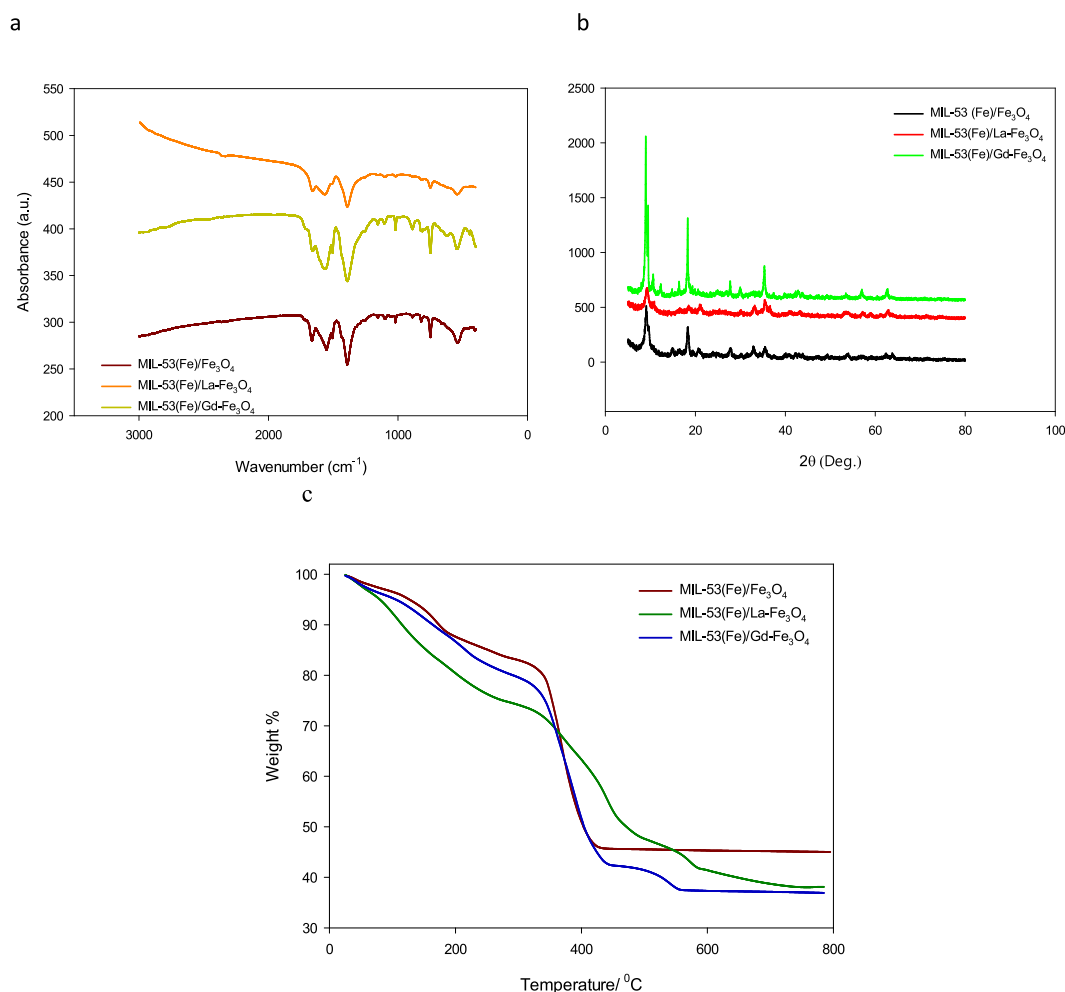


Fig. 2. (a) FTIR absorption spectra; (b) diffraction patterns; (c) TG curves of MIL-53 (Fe)/Fe<sub>3</sub>O<sub>4</sub>; MIL-53(Fe)/ La-Fe<sub>3</sub>O<sub>4</sub> and MIL-53(Fe)/ Gd-Fe<sub>3</sub>O<sub>4</sub>.

which confirms the successful synthesis of MIL-53(Fe) (Ali et al., 2023); (Horcajada et al., 2008) ; (Abdollahi-Basir et al., 2019) . As shown in Fig. 2b, the addition La or Gd has no effect on the crystals of MOFs and the characteristic peaks of MIL-53 (Fe)/La-Fe<sub>3</sub>O<sub>4</sub> and MIL-53 (Fe)/Gd-Fe<sub>3</sub>O<sub>4</sub> appeared in the same position as the original sample (Ali et al., 2023). The diffraction lines at  $2\theta > 30^\circ$ , (JCPDS card No. 79-0419), were in accordance with the cubic phase of Fe<sub>3</sub>O<sub>4</sub> (Ali et al., 2023); (Ahmed et al., 2013) ; (Ali et al., 2017) . The analysis results of XRD were accordance with the FTIR result.

Thermal stability is a vital feature of MOFs. The stability of MILs was investigated by applying thermogravimetric analysis (TGA) in an inert atmosphere (N<sub>2</sub>) under heating rate of 10 °C min<sup>-1</sup>. The thermal curves of the MIL-53(Fe) /Fe<sub>3</sub>O<sub>4</sub> series show three main weight loss steps, Fig. 2.c. The first drop appeared between 100° C and 160° C and was related to the loss of water inside the pores and the residual DMF. The second weight loss at approximately 400°C may be related to the complete collapse of the MOFs to their original TPA and Fe (III) ions. The third peak approximately 500° C was related to the transformation of magnetic particles into the amorphous Fe<sub>2</sub>O<sub>3</sub> phase (Martínez-Navarro et al., 2020).

the nitrogen adsorption-desorption isotherms curves of MILs confirm their mesoporous structure of them by having type IV isotherm. The BET surface area of pristine MIL-53 (Fe)/Fe<sub>3</sub>O<sub>4</sub> is 20.82 m<sup>2</sup>/g, Table 1. This value is larger than the reported result of MIL-53(Fe) at 14 m<sup>2</sup>/g (Fan et al., 2019) but it is still low. This may be due to the nature of MIL-53 (Fe) which is flexible and has a breathing effect, to open its pores only in the presence of a guest molecule (Liang et al., 2019). The low

Table 1

BET surface area, Average Crystalline Size, pore volume values for of MIL-53 (Fe) samples.

Sample	BET Specific Surface Area, SBET (m <sup>2</sup> .g <sup>-1</sup> )	Average Crystalline Size (nm)	Pore Volume (cm <sup>3</sup> .g <sup>-1</sup> )
MIL-53 (Fe)/ Fe <sub>3</sub> O <sub>4</sub>	20.82	8.16	0.062
MIL-53 (Fe)/ Gd-Fe <sub>3</sub> O <sub>4</sub>	29.11	32.25	0.101
MIL-53 (Fe)/ La-Fe <sub>3</sub> O <sub>4</sub>	54.18	8.60	0.151

surface area observed on MIL-53 (Fe)/Gd-Fe<sub>3</sub>O<sub>4</sub> shows that it has almost closed pores with no accessible porosity to N<sub>2</sub> gas. This confirms that these flexible structure materials have an exceptional property, their ability to adapt their pore opening to accommodate the guest species. The flexibility occurs through the tilting of the organic linkers without significantly altering the coordination environment around the cation (Grape et al., 2019).

### 3.2. Electrocatalytic activities toward HER

The motivation for utilizing the lanthanide doped MIL-53 (Fe) with magnetite precursor catalysts was to improve the reduction current response and limit the overpotential. The HER performances of MIL-53 (Fe)/Fe<sub>3</sub>O<sub>4</sub>, MIL-53 (Fe)/La-Fe<sub>3</sub>O<sub>4</sub>, and MIL-53(Fe)/Gd-Fe<sub>3</sub>O<sub>4</sub> were tested in 0.5 mol/L H<sub>2</sub>SO<sub>4</sub> on the GC and Au electrodes. Electrochemical

reduction of hydrogen on the magnetite-based MIL derivatives was investigated with CV by sweeping the potential from 1.0 to  $-0.5$  V at a scan rate of  $100 \text{ mV s}^{-1}$ . The reduction peak current and peak potential were determined from the 8th cycle as it reached a steady value. As shown in Fig. 3 a,b Au/MIL-53(Fe)/Gd- $\text{Fe}_3\text{O}_4$  demonstrated the highest HER activity of all the electrodes on the Au base electrodes and required an overpotential of  $-0.5$  V with a maximum reduction current of  $62.56 \text{ mA cm}^{-2}$ . In contrast, a good reductive peak of  $185 \times 10^{-3} \text{ mA cm}^{-2}$  at  $0.057 \text{ V}$  was observed for GCE/MIL-53 (Fe)/La- $\text{Fe}_3\text{O}_4$ , Table 2. CV curves of bare GC or Au electrode were used as a control to determine any activity of the electrodes before being modified by MIL-53 (Fe) catalysts. These data demonstrate that hydrogen was not electro-reduced on them. The high drive cathodic currents of the lanthanide doped MIL-53 (Fe)/ $\text{Fe}_3\text{O}_4$  on Au as the base electrode clearly demonstrate the effect of the main metal electrode on the electrical process occurring at the surface.

The polarization technique is a systematic and effective method to investigate the electrochemical activity of the electrocatalysts. A set of Tafel lines recorded in test solution at the potential region of hydrogen evolution for base electrodes modified MILs together with unmodified base electrodes. Fig. 3 c,d shows that the presence of the MILs modifier resulted in an increase in the electrocatalytic activity toward HER by over 100 times. The GCE and Au modified with the MIL catalysts display two potential regions related to HER. At low overpotentials, the curves are characterized by a well-defined Tafel behavior. By contrast, at higher overpotentials, a significant deviation from Tafel behavior was recorded. The change in Tafel slope due to the existence of two Tafel regions has already been reported in the literature (de Chialvo and Chialvo, 1994); (Xiao et al., 2014). Thus, a change in the HER mechanism has been suggested as one possible explanation. A possible reason

**Table 2**

Summary of the catalytic activity of the MILs electrocatalysts in  $0.5 \text{ mol/L H}_2\text{SO}_4$ .

Catalyst Type	Cyclic Voltammetry		Linear Tafel Polarization		
	I (mA/cm <sup>2</sup> )	-E (mV)	-b (mV/dec)	$-j_0$ (mA/cm <sup>2</sup> )	$-j$ (mA/cm <sup>2</sup> ) at $-400 \text{ mV}$
Bare Au	1.60	–	81	10.38	0.113
Au/MIL-53 (Fe)/ $\text{Fe}_3\text{O}_4$	10.67	500	82	12.91	0.167
Au/MIL-53 (Fe)/La- $\text{Fe}_3\text{O}_4$	18.14	500	82	12.93	1.580
Au/MIL-53 (Fe)/Gd- $\text{Fe}_3\text{O}_4$	62.56	500	81	12.95	18.529
Bare GCE	–	–	166	1.36	0.007
GCE/MIL-53 (Fe)/ $\text{Fe}_3\text{O}_4$	0.071	97	182	8.41	0.080
GCE/MIL-53 (Fe)/La- $\text{Fe}_3\text{O}_4$	0.185	40	166	8.71	0.213
GCE/MIL-53 (Fe)/Gd- $\text{Fe}_3\text{O}_4$	0.184	57	164	8.56	0.173

for the observed diffusion-like shape of the Tafel lines be cause of mass-transport limitations through pores on the catalyst surface (Xiao et al., 2014); (Xu et al., 2022); (Zhang et al., 2023) which have been suggested as possible reason for the observed diffusion-like shape of the Tafel lines.

Notably, the exchange current density is frequently used for the characterization of electrocatalytic activity. A common way of comparing the electrocatalytic activity of HER electrocatalysts is to fix the overpotential (i.e., hydrogen production power) and then compare the resulting current density values, that reveal the amount of hydrogen that would be produced by each catalyst. The measured current densities

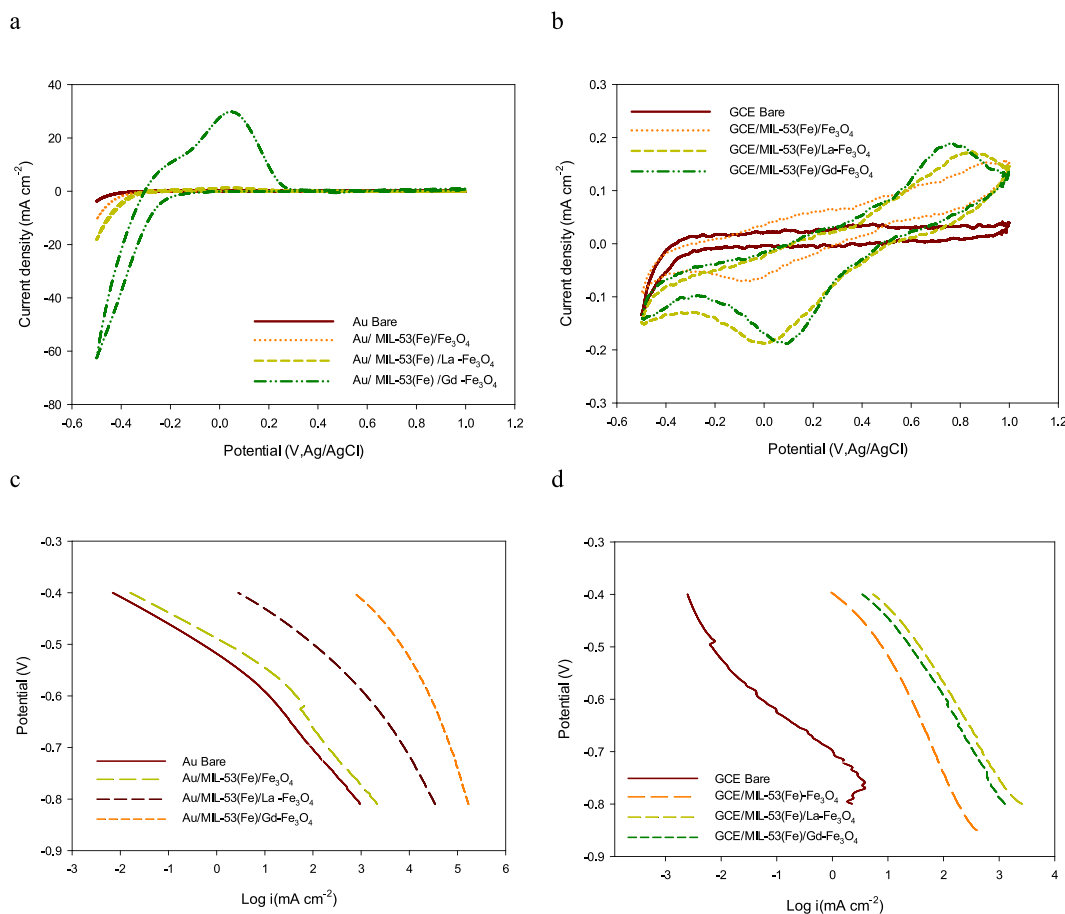
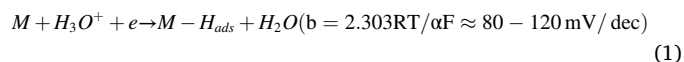


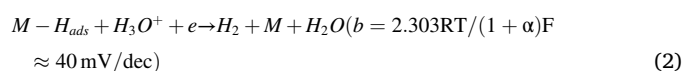
Fig. 3. a,b) her cyclic voltammetry curves; c,d) the corresponding polarization curves of modified mils on au or gc electrodes respectively.

$j$  (mA/cm<sup>2</sup>) at  $-400$  mV, Table 2, again confirm that Tafel lines measurements reveal the same trend of HER electrocatalytic activity observed in CV measurements. The Tafel slope known as an intrinsic property of the catalysts, can be used to evaluate their catalytic activity and is determined by the rate limiting step of the HER (Du et al., 2018); (Deng et al., 2019). The shape of the Tafel curves in Fig. 3 suggests a diffusion-limited reaction controlled by mass transport through the narrow pores in the multilayer structures of the catalysts (Galal et al., 2010); (Yin et al., 2018).

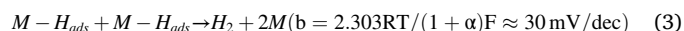
According to hydrogen binding energy (HBE), there are two possible reaction mechanisms for HER in acidic media (Tang et al., 2012). The first step in both mechanisms is the **Volmer reaction**, where  $H_3O^+$  adsorption occurs after an electron transfer on the surface of the electrodes:



The next step is followed by either a Heyrovsky reaction (Volmer–Heyrovsky mechanism)



or by a **Tafel reaction** involving the chemical recombination of two  $H_{ads}$  atoms (Volmer–Tafel mechanism):



For the value of  $b$  given in each reaction,  $R$  is the ideal gas constant,  $T$  is the absolute temperature,  $\alpha = 0.5$  is the symmetry coefficient, and  $F$  is the Faraday constant. The Tafel slope for the Au/MIL-53(Fe)/Gd-Fe<sub>3</sub>O<sub>4</sub>

and GCE/MIL-53(Fe)/La-Fe<sub>3</sub>O<sub>4</sub> catalyst samples was 81–166 mV.dec<sup>-1</sup>. This was replicated for all of the catalysts studied, suggesting that the HER followed the Volmer-Tafel mechanism influenced by both electron transfer and hydrogen adsorption. Within this framework, this outcome confirms that the magnetite (Fe<sub>3</sub>O<sub>4</sub>) nanoparticles not only enhanced the conductivity but also it is an effective catalyst surface where binding H was too weak, disfavoring adsorption (i.e., the Volmer step) (Nivetha et al., 2020); (Kuo et al., 2022).

To further identify the catalysts' intrinsic activity toward HER, the double-layer capacitance ( $C_{dl}$ ) was probed to estimate the electrochemically active surface area (ECSA) which is closely related to the number of exposed active sites and the corresponding intrinsic activity. The CV curves of modified MILs with different scan rates are shown in Fig. 4a,b. As presented in Fig. 4c,d, Au/MIL-53(Fe)/Gd-Fe<sub>3</sub>O<sub>4</sub> and GCE/MIL-53(Fe)/La-Fe<sub>3</sub>O<sub>4</sub> exhibited a slope ( $C_{dl}$ ) of 32.22 mF cm<sup>-2</sup> and 2.74 mF cm<sup>-2</sup> and ECSA 1611 and 1370 cm<sup>-2</sup>, respectively, considerably larger than those other MILs and further confirmed the considerably higher intrinsic activity of these two compounds and the effect of the base electrode.

The observation that the performance of a catalyst is generally better when loaded on an Au electrode than on a GCE can be attributed to several factors: **First**, Au is known for its excellent electrical conductivity, which facilitates efficient charge transfer between the catalyst and the electrode. This promotes better electrochemical reactions and enhances the overall catalytic performance. Conversely, glassy carbon, has relatively lower electrical conductivity, leading to less efficient charge transfer and lower catalytic activity (Xu et al., 2019). **Second**, Au electrodes often possess a highly ordered and clean surface, which provides a well-defined and uniform environment for catalyst deposition. This allows for better control over the catalyst loading and

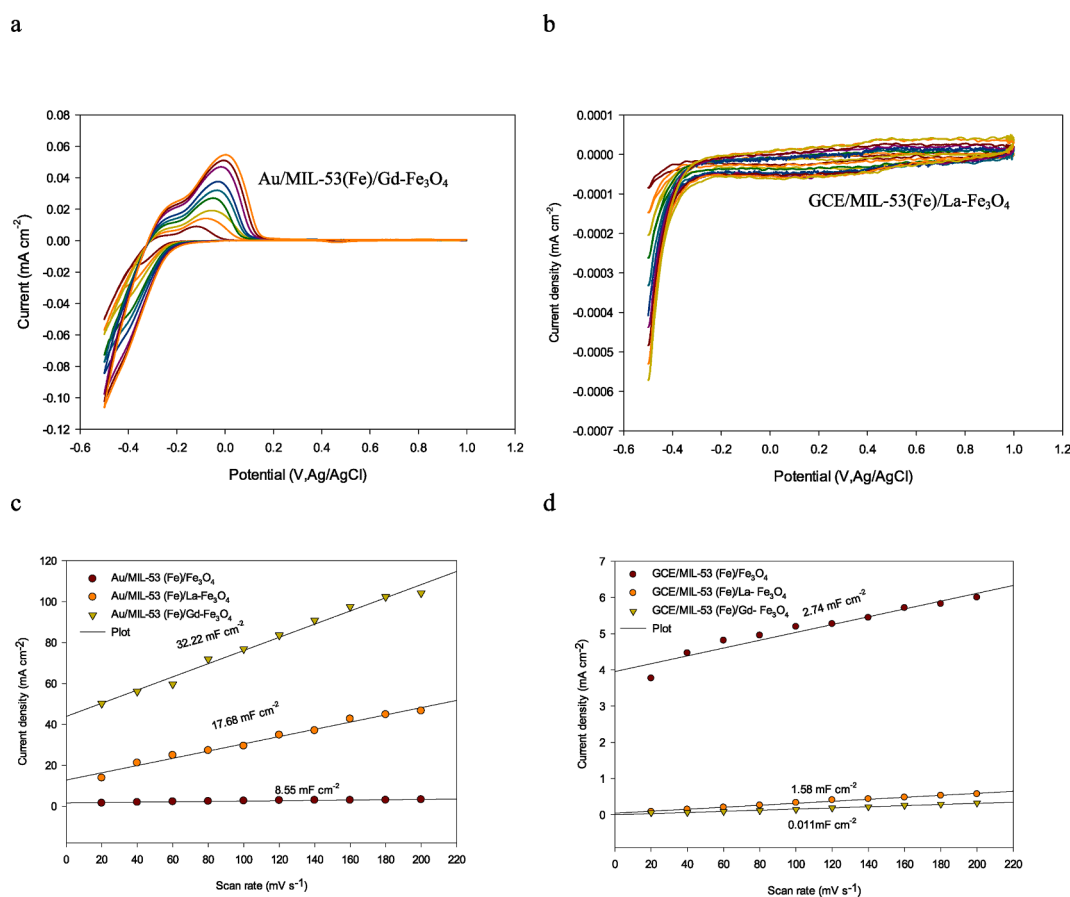


**Fig. 4.** a,b, cyclic voltammograms of, Au/MIL-53(Fe)/Gd-Fe<sub>3</sub>O<sub>4</sub> and GCE/MIL-53(Fe)/La-Fe<sub>3</sub>O<sub>4</sub>, (c,d) the differences in current density variation ( $j_a-j_c$ ) at an overpotential of  $-0.5$  V plotted against scan rate.

promotes a higher density of active sites, leading to enhanced catalytic activity. However, glassy carbon, may have a more irregular and less controlled surface, which can result in less efficient catalyst deposition and a lower density of active sites (Fernandes et al., 2022). **Third**, according to stability, Au is generally more chemically stable than glassy carbon. Au exhibits excellent resistance to corrosion and oxidative processes, which ensures the long-term stability and durability of the catalyst on the electrode surface. By contrast, glassy carbon, can be susceptible to chemical degradation and surface modifications, which may affect the stability and performance of the catalyst over time (Fernandes et al., 2022).

### 3.3. Stability

The stability of electrocatalysts is also a relevant factor when judging the HER performance of a catalyst. Continuous 50 cycle CV scanning was conducted with a scan rate of  $100 \text{ mV s}^{-1}$ , and a negligible difference could be observed after 9th cycle at  $-0.5 \text{ V}$  (Fig. 5). The high stability of Au/MIL-53(Fe)/Gd- $\text{Fe}_3\text{O}_4$  and GCE/MIL-53(Fe)/La- $\text{Fe}_3\text{O}_4$  was observed at a current density extremely close to that CV. There was a slight current shift (less than 0.13 and 0.001 mA respectively) for catalysts Au/MIL-53(Fe)/Gd- $\text{Fe}_3\text{O}_4$  and GCE/MIL-53(Fe)/La- $\text{Fe}_3\text{O}_4$ . This indicates that both catalysts exhibited better durability, stability and a substantially low rate of surface poisoning under acidic conditions.

### 3.4. Electrode resistance

The creation of resistance to the ionic and charge transport in the electrolyte during the electrochemical measurement is the most effective actor in determining the electrocatalytic activity of a catalyst. It can be as used a barrier during water electrolysis. EIS is a relevant technology to study the interface properties of the electrode and the kinetics of HER on the surface of the catalysts (Esmailzadeh et al., 2020); (Liao et al., 2022); (Qi et al., 2023).

To determine the interface behavior of the lanthanide doped MIL-53 (Fe) catalysts and the kinetic of HER, the EIS test was done and the Nyquist data in overpotentials of  $-0.5 \text{ V}$  (vs. Ag/AgCl) were recorded and shown in Fig. 6. As can be observed, for all samples the Nyquist plots consist of two-time constants overlapped by semicircles. Therefore, an equivalent circuit with two-time constants can be discerned within the studied frequency range. To obtain a physical picture of the electrode/electrolyte interface and the processes occurring at the electrode surface, experimental EIS data were modeled using *Gamry Echem Analyst* software and an electrical equivalent circuit (EEC). The equivalent circuit model shown in Fig. 6c has been used to describe the response of the HER on porous electrodes (Wu et al., 2020); (Tan et al., 2021); (Wang et al., 2021).

In the EEC model each element stands for a different meaning. Rs is the solution resistance. CPE1 is related to the double layer capacitance

( $C_{dl}$ ). R1 is the charge transfer resistance. CPE2 is the constant phase element of the porous pseudo-capacitance ( $C_p$ ), and R2 is associated with the diffusion process in the pores or the resistance of the adsorbed intermediate  $\text{H}_{ads}$  (Wu et al., 2020); (Tan et al., 2021).

The first semicircle regarding the high frequency region (CPE1,R1) is related to the charge-transfer kinetics of the HER on the electrode. CPE1 increased and the diameter of the semicircle R1 decreased regularly which reflects the need to minimize the electron transfer resistance from MOFs to  $\text{H}^+$  and accelerate proton transport, Table 3. Contrary to the behavior of CPE1, the value of CPE2 was shown to increase. At the same time, the value of R2 decreased, which is beneficial for elevating the diffusion of  $\text{H}_2$  gas through the pores. This is a typical behavior related to the porosity of the electrode surface (Liu et al., 2019). The lanthanide doped MIL-53 (Fe) catalyst behavior on the Au and GC electrodes above is in agreement with CV data.

In general, benefiting from the unique porous morphology, the  $\text{Fe}_3(\text{Fe}_2\text{C}_6\text{H}_4(\text{CO}_2\text{H})_2)_2$  facilitates mass transfer during the electrocatalytic process (Fig. 6d). As it is known theoretically, the binding affinity of a proton to achieve electron transfer is provided only on unsaturated sites. the present study, the moiety of  $\text{Fe}_3(\text{Fe}_2\text{-lanthanide})\text{-C}_6\text{H}_4(\text{CO}_2\text{H})_2$  has a higher unsaturation degree with large pores in comparison with  $\text{Fe}_3(\text{Fe}_2\text{-C}_6\text{H}_4(\text{CO}_2\text{H})_2)_2$ .

Lanthanide cations and the delocalized  $\pi$ -electron system within certain ligands can indeed provide a strongly active center for electron transfer. The presence of the lanthanide cation and the  $\pi$ -electron system allows for efficient electronic communication and facilitates electron transfer processes. When lanthanide carboxylate complexes with high surface area are exposed to an acidic environment, protonation of the carboxylate ligands can occur. This protonation can increase the electron density on O<sub>2</sub> atoms of the carboxylate groups, making them more electron-rich. Thus, electrons from the carboxylate ligands to the  $\text{H}^+$  cation to produce  $\text{H}_2$  gas more favorable.

### 3.5. Activation energy of HER

Before the reactants can be converted into products, the free energy of the system must overcome the activation energy ( $E_a$ ) for the reaction. A temperature increase, i.e., enhancement of the thermal motion, leads to an increase in the distance up to which  $\text{H}_3\text{O}^+$  may approach the catalyst surface and a corresponding exchange current increase. Fig. 7(a-f) a set of Tafel curves recorded on Au or GC electrodes modified with MIL-53(Fe)/ $\text{Fe}_3\text{O}_4$  derivatives at various temperatures demonstrate that the exchange current followed the Arrhenius equation.

The Arrhenius equation allows us to calculate activation energies, thus, judging the effectiveness of the catalyst used to accelerate a reaction. The calculated activation energy values for MIL-53(Fe)/ $\text{Fe}_3\text{O}_4$  catalysts are recorded in Table 3.

The lower activation energy calculated for the hydrogen ion discharge ( $E_a = 11.84$  and  $16.56 \text{ kJ/mol}$ ) on Au/MIL-53 (Fe)/Gd- $\text{Fe}_3\text{O}_4$

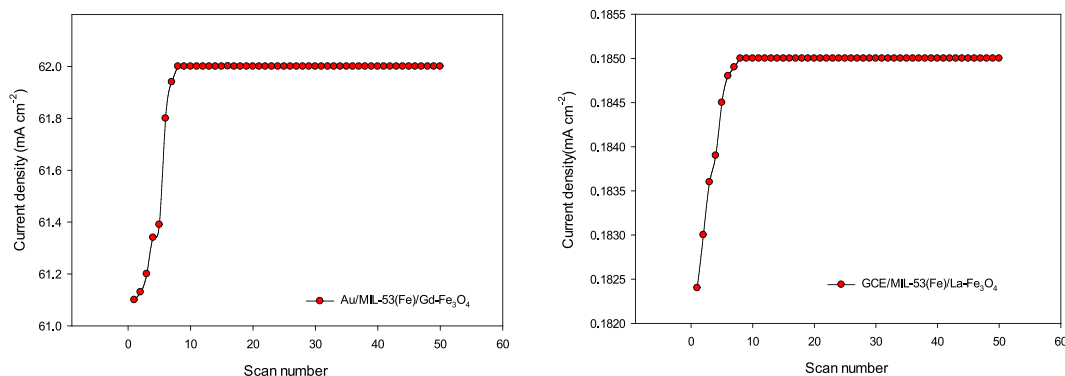
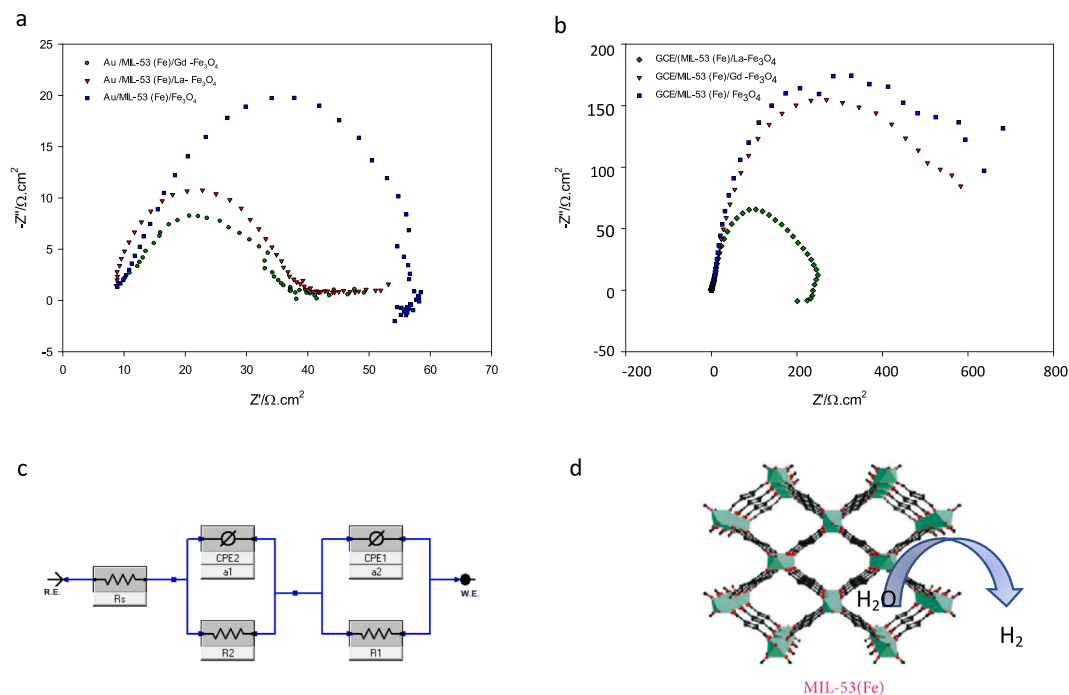


Fig. 5. The stability of Au/MIL-53(Fe)/Gd- $\text{Fe}_3\text{O}_4$  and GCE/MIL-53(Fe)/La- $\text{Fe}_3\text{O}_4$  catalysts by Continuous 50 cycles CV scanning.



**Fig. 6.** (a,b) AC impedance of modified MILs on Au or GC electrodes respectively, (c) equivalent circuit model, (d) Electrochemical diagram of  $\text{Fe}_3(\text{Fe}_2\text{C}_6\text{H}_4(\text{CO}_2\text{H})_2)_2$  nanosheets toward HER.

**Table 3**

Parameter for electrocatalytic activity and activation energy variation for different catalysts.

Different Sensors	Parameter (unit)							Activation Energy ( $E_a$ ), kJ/mol
	$R_s$ ( $\Omega\text{cm}^2$ )	$R_1$ ( $\Omega\text{cm}^2$ )	$\text{CPE1} \times 10^3 \mu\text{F cm}^{-2}$	m	$R_2$ ( $\Omega\text{cm}^2$ )	n	$\text{CPE2} \times 10^6 \mu\text{F cm}^{-2}$	
Au/MIL-53 (Fe)/ $\text{Fe}_3\text{O}_4$	1.5	25.32	54.51	0.22	56.20	0.99	2.37	20.89
Au /MIL-53 (Fe)/La- $\text{Fe}_3\text{O}_4$	2.4	15.23	28.90	0.24	44.35	0.96	3.22	16.01
Au /MIL-53 (Fe)/Gd - $\text{Fe}_3\text{O}_4$	3.7	11.21	9.19	0.31	39.27	0.91	4.16	11.84
GCE/MIL-53 (Fe)/ $\text{Fe}_3\text{O}_4$	1.03	79.60	99.91	0.37	149.09	0.72	616.61	26.77
GCE/(MIL-53 (Fe)/La- $\text{Fe}_3\text{O}_4$	1.23	69.48	105.12	0.52	124.40	0.71	232.18	16.56
GCE/MIL-53 (Fe)/Gd - $\text{Fe}_3\text{O}_4$	2.1	77.73	103.5	0.50	139.37	0.71	535.90	19.24

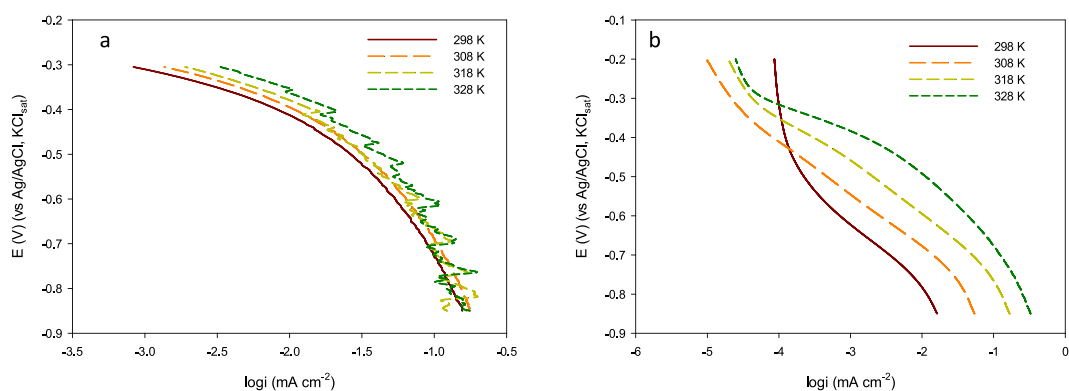


**Fig. 7.** Linear Tafel polarization curves for the HER recorded on modified MILs (a) Au and (b) GC electrodes respectively in 0.5 mol/L  $\text{H}_2\text{SO}_4$  at various temperatures.

and GCE/MIL-53 (Fe)/La- $\text{Fe}_3\text{O}_4$  catalysts compared with the energy on other MILs indicates that active sites at these catalyst surfaces are considerably more active. The presence of lanthanides such as La and Gd creates hybrid nanomaterials that improve the proton reductive dopant into MIL-53(Fe)/  $\text{Fe}_3\text{O}_4$  and modify its energy gap properties. There are few studies that calculate the activation energy of reactions on MOFs. Aguila *et al.* (Aguila *et al.*, 2018) inserted a flexible polymer into a (MOF, MIL-101(Cr) host. The advantages of both components work

synergistically to create a composite that efficiently fixes carbon dioxide to transform various epoxides into cyclic carbonate. This approach was taken to determine the effect that adding a cooperative MOF catalyst has on the activation energy of a reaction. The activation energies of kinetic rates of epichlorohydrin conversion for catalysts MIL-101-IP (induce polymerization) when compared with the physical mixture (MIL-101 + IP) under the same conditions for 25 °C and 40 °C were 63.6 kJ mol<sup>-1</sup> and 91.6 kJ mol<sup>-1</sup> respectively. This indicates the advantages of

including the ionic polymer within the pores of MIL-101.

#### 4. Conclusion

In summary, we have demonstrated the Fe-based MOF with a modified precursor of magnetite ( $\text{Fe}_3\text{O}_4$ ) to reveal improved electrocatalytic performance for HER functions in acidic media. The crystalline characteristics, chemical structure, thermal stability and nanostructure morphology of MILs were studied using XRD, FTIR, TGA and SEM. The introduction of lanthanide into the precursor ( $\text{Fe}_3\text{O}_4$ ) results in improved electrical characteristics in the resulting MILs. Au/MIL-53 (Fe)/Gd- $\text{Fe}_3\text{O}_4$  electrocatalyst displayed excellent HER activity compared to GCE/MIL-53(Fe)/La- $\text{Fe}_3\text{O}_4$  with overpotential values of  $-0.5$  V and a maximum reduction current of  $62.56$  mA  $\text{cm}^{-2}$ . The data also highlight the correlation between the choice of the base metal electrode (Au or GC) and catalysts activity. The bimetallic precursor (Fe-La) or (Fe-Gd) offered improved conductivity and enhanced charge transfer capability to promote gas evolution kinetics (as visualized through the respective Tafel slopes, impedance results and stability). The improved performance of the Au/MIL-53(Fe)/Gd- $\text{Fe}_3\text{O}_4$  catalyst and its low activation energy ( $E_a = 11.84$  kJ/mol) owing to base metal. Au electrode often offers advantages in catalytic performance due to their electrical conductivity, clean surface and stability. The experimental results reveal new great opportunities for a more targeted search for highly efficient MOF electrocatalysts and other electrode materials for water electrolysis technology in the future.

#### Declaration of competing interest

The authors declare the following financial interests/personal relationships which may be considered as potential competing interests: KHADIJAH Emran reports administrative support was provided by Taibah University. Khadijah Emran reports administrative support was provided by Taibah University. If there are other authors, they declare that they have no known competing financial interests or personal relationships that could have appeared to influence the work reported in this paper.

#### Acknowledgements

The authors would like to thank the technicians Miss. Reem A-Rashidi and Miss. Ro'a AboSaif for conducting surface measurements of the study samples.

#### References

- Abdalla, A.M., Hossain, S., Nisfindy, O.B., Azad, A.T., Dawood, M., Azad, A.K., 2018. Hydrogen production, storage, transportation and key challenges with applications: A review. *Energ. Convers. Manage.* 165, 602–627. <https://doi.org/10.1016/j.enconman.2018.03.088>.
- Abdollahi-Basir, M.H., Shirini, F., Tajik, H., Ghasemzadeh, M.A., 2019. MIL-53 (Fe): Introduction of a new catalyst for the synthesis of Pyrimido [4, 5-d] pyrimidine derivatives under solvent-free conditions. *J. Mol. Struct.* 1197, 318–325. <https://doi.org/10.1016/j.molstruc.2019.07.065>.
- Abu-Dief, A.M., Alrashedee, F.M.M., Emran, K.M., Al-Abdulkarim, H.A., 2022. Development of some magnetic metal-organic framework nano composites for pharmaceutical applications. *Inorg. Chem. Commun.* 138, 109251 <https://doi.org/10.1016/j.inoche.2022.109251>.
- Aguila, B., et al., 2018. Lower activation energy for catalytic reactions through host-guest cooperation within metal-organic frameworks. *Angew. Chem.* 130 (32), 10264–10268. <https://doi.org/10.1002/ange.201803081>.
- Ahmed, M.A., Ali, S.M., El-Dek, S.I., Galal, A., 2013. Magnetite-hematite nanoparticles prepared by green methods for heavy metal ions removal from water. *Mater. Sci. Eng. B* 178 (10), 744–751. <https://doi.org/10.1016/j.mseb.2013.03.011>.
- Ai, L., Li, L., Zhang, C., Fu, J., Jiang, J., 2013. "MIL-53 (Fe): a metal-organic framework with intrinsic peroxidase-like catalytic activity for colorimetric biosensing". *Chem. Eur. J.* 19 (45), 15105–15108. <https://doi.org/10.1002/chem.201303051>.
- Ali, S.M., Emran, K.M., Al-Oufi, A.L.L., 2017. Adsorption of organic pollutants by nano-conducting polymers composites: Effect of the supporting nano-oxide type. *J. Mol. Liq.* 233, 89–99. <https://doi.org/10.1016/j.molliq.2017.03.006>.

- Ali, S.M., Galal, A., Atta, N.F., 2017. Toxic heavy metal ions removal from wastewater by nano-magnetite: Case study Nile river water. *Egypt. J. Chem.* 60 (4), 601–612. <https://doi.org/10.21608/ejchem.2017.3583>.
- Ali, S.M., Emran, K.M., Alrashedee, F.M.M., 2023. Removal of organic pollutants by lanthanide-doped MIL-53 (Fe) metal-organic frameworks: Effect of dopant type in magnetite precursor. *J. Rare Earths* 41 (1), 140–148. <https://doi.org/10.1016/j.jre.2022.01.012>.
- Alqadami, A.A., Naushad, M., Alothman, Z.A., Ghfar, A.A., 2017. Novel metal-organic framework (MOF) based composite material for the sequestration of U (VI) and Th (IV) metal ions from aqueous environment. *ACS Appl. Mater. Interfaces* 9 (41), 36026–36037. <https://doi.org/10.1021/acsami.7b10768>.
- Amiinu, I.S., et al., 2017. Multifunctional Mo-N/C@ MoS<sub>2</sub> electrocatalysts for HER, OER, ORR, and Zn-air batteries. *Adv. Funct. Mater.* 27 (44), 1702300. <https://doi.org/10.1002/adfm.201702300>.
- Amiinu, I.S., et al., 2018. From 3D ZIF nanocrystals to Co-Nx/C nanorod array electrocatalysts for ORR, OER, and Zn-air batteries. *Adv. Funct. Mater.* 28 (5), 1704638. <https://doi.org/10.1002/adfm.201704638>.
- Carmo, M., Fritz, D.L., Mergel, J., Stolten, D., 2013. A comprehensive review on PEM water electrolysis. *Int. J. Hydrogen Energy* 38 (12), 4901–4934. <https://doi.org/10.1016/j.ijhydene.2013.01.151>.
- Chen, J., et al., 2019. Co-Fe-P nanotubes electrocatalysts derived from metal-organic frameworks for efficient hydrogen evolution reaction under wide pH range. *Nano Energy* 56, 225–233. <https://doi.org/10.1016/j.nanoen.2018.11.051>.
- Cheng, F., et al., 2021. In situ identification of the electrocatalytic water oxidation behavior of a nickel-based metal-organic framework nanoarray. *Mater. Horiz.* 8 (2), 556–564. <https://doi.org/10.1039/D0MH01757D>.
- Cheng, W., Zhang, H., Luan, D., Lou, X.W., 2021. "Exposing unsaturated Cu1-O2 sites in nanoscale Cu-MOF for efficient electrocatalytic hydrogen evolution". *Sci. Adv.* 7 (18), eabg2580. <https://doi.org/10.1126/sciadv.abg2580>.
- Chi, J., Yu, H., 2018. Water electrolysis based on renewable energy for hydrogen production. *Chin. J. Catal.* 39 (3), 390–394. [https://doi.org/10.1016/S1872-2067\(17\)62949-8](https://doi.org/10.1016/S1872-2067(17)62949-8).
- de Chialvo, M.R.G., Chialvo, A.C., 1994. Hydrogen evolution reaction: Analysis of the Volmer-Heyrovsky-Tafel mechanism with a generalized adsorption model. *J. Electroanal. Chem.* 372 (1–2), 209–223. [https://doi.org/10.1016/0022-0728\(93\)03043-O](https://doi.org/10.1016/0022-0728(93)03043-O).
- Deng, Y., Ye, C., Chen, G., Tao, B., Luo, H., Li, N., 2019. EDTA-assisted hydrothermal synthesis of flower-like CoSe<sub>2</sub> nanorods as an efficient electrocatalyst for the hydrogen evolution reaction. *J. Energy Chem.* 28, 95–100. <https://doi.org/10.1016/j.jechem.2018.01.022>.
- Do, H.H., et al., 2022. Metal-organic-framework based catalyst for hydrogen production: Progress and perspectives. *Int. J. Hydrogen Energy* 47 (88), 37552–37568. <https://doi.org/10.1016/j.ijhydene.2022.01.080>.
- Du, J., Wang, X., Li, C., Liu, X.-Y., Gu, L., Liang, H.-P., 2018. Hollow Rh nanoparticles with nanoporous shell as efficient electrocatalyst for hydrogen evolution reaction. *Electrochim. Acta* 282, 853–859. <https://doi.org/10.1016/j.electacta.2018.06.126>.
- Esmailzadeh, S., Shahrabadi, T., Darband, G.B., Yaghoubinezhad, Y., 2020. Pulse electrodeposition of nickel selenide nanostructure as a binder-free and high-efficient catalyst for both electrocatalytic hydrogen and oxygen evolution reactions in alkaline solution. *Electrochim. Acta* 334, 135549. <https://doi.org/10.1016/j.electacta.2019.135549>.
- Fan, L., et al., 2019. Fe-MOF derived jujube pit like Fe<sub>3</sub>O<sub>4</sub>/C composite as sulfur host for lithium-sulfur battery. *Electrochim. Acta* 295, 444–451. <https://doi.org/10.1016/j.electacta.2018.08.107>.
- Farinotti, D., Round, V., Huss, M., Compagno, L., Zekollari, H., 2019. Large hydropower and water-storage potential in future glacier-free basins. *Nature* 575 (7782), 341–344. <https://doi.org/10.1038/s41586-019-1740-z>.
- Fernandes, P.M.V., Pereira, C.M., Campiña, J.M., Silva, A.F., 2022. Graphene-modified glassy carbon electrodes: Correlations between electrochemical performance, film morphology and composition. *Int. J. Electrochem. Sci.* 17 (3), 220347 <https://doi.org/10.20964/2022.03.47>.
- Galal, A., Darwish, S.A., Atta, N.F., Ali, S.M., Abd El Fatah, A.A., 2010. Synthesis, structure and catalytic activity of nano-structured Sr-Ru-O type perovskite for hydrogen production. *Appl. Catal. A: Gen.* 378 (2), 151–159. <https://doi.org/10.1016/j.apcata.2010.02.015>.
- Grape, E.S., et al., 2019. Breathing metal-organic framework based on flexible inorganic building units. *Cryst. Growth Des.* 20 (1), 320–329. <https://doi.org/10.1021/acs.cgd.9b01266>.
- Horcajada, P., et al., 2008. Flexible porous metal-organic frameworks for a controlled drug delivery. *J. Am. Chem. Soc.* 130 (21), 6774–6780. <https://doi.org/10.1021/ja710973k>.
- Huang, H., Zhao, Y., Bai, Y., Li, F., Zhang, Y., Chen, Y., 2020. Conductive metal-organic frameworks with extra metallic sites as an efficient electrocatalyst for the hydrogen evolution reaction. *Adv. Sci.* 7 (9), 2000012. <https://doi.org/10.1002/advs.202000012>.
- O. Inderwildi, C. Zhang, X. Wang, and M. Kraft, "The impact of intelligent cyber-physical systems on the decarbonization of energy," *Energy and Environmental Science*, vol. 13, no. 3. Royal Society of Chemistry, pp. 744–771, Mar. 01, 2020. doi: 10.1039/c9ee01919g.
- Kuo, D.-Y., Nishiwaki, E., Rivera-Maldonado, R.A., Cossairt, B.M., 2022. The role of hydrogen adsorption site diversity in catalysis on transition-metal phosphide surfaces. *ACS Catal.* 13, 287–295. <https://doi.org/10.1021/acscatal.2c04936>.
- Liang, Z., Qiu, T., Gao, S., Zhong, R., Zou, R., 2022. Multi-scale design of metal-organic framework-derived materials for energy electrocatalysis. *Adv. Energy Mater.* 12 (4), 2003410. <https://doi.org/10.1002/aenm.202003410>.

- Liang, Y., Zhang, L., Zhang, Y., 2019. Well-defined materials for high-performance chromatographic separation. *Annu. Rev. Anal. Chem.* 12, 451–473. <https://doi.org/10.1146/annurev-anchem-061318-114854>.
- Liao, J., et al., 2022. MoS<sub>2</sub> supported on Er-MOF as efficient electrocatalysts for hydrogen evolution reaction. *J. Alloy. Compd.* 898, 162991 <https://doi.org/10.1016/j.jallcom.2021.162991>.
- Liu, T., et al., 2019. CoP-doped MOF-based electrocatalyst for pH-universal hydrogen evolution reaction. *Angew. Chem.* 131 (14), 4727–4732. <https://doi.org/10.1002/ange.201901409>.
- Liu, N., et al., 2020. Magnetic Fe<sub>3</sub>O<sub>4</sub>@ MIL-53 (Fe) nanocomposites derived from MIL-53 (Fe) for the photocatalytic degradation of ibuprofen under visible light irradiation. *Mater. Res. Bull.* 132, 111000 <https://doi.org/10.1016/j.materresbull.2020.111000>.
- Lu, X.F., Chen, Y., Wang, S., Gao, S., Lou, X.W., 2019. Interfacing manganese oxide and cobalt in porous graphitic carbon polyhedrons boosts oxygen electrocatalysis for Zn–air batteries. *Adv. Mater.* 31 (39), 1902339. <https://doi.org/10.1002/adma.201902339>.
- Lu, X.F., Yu, L., Lou, X.W., 2019. Highly crystalline Ni-doped FeP/carbon hollow nanorods as all-pH efficient and durable hydrogen evolving electrocatalysts. *Sci. Adv.* 5 (2), eaav6009. <https://doi.org/10.1126/sciadv.aav6009>.
- Martínez-Navarro, B., Sanchis, R., Asedegbega-Nieto, E., Solsona, B., Ivars-Barceló, F., 2020. (Ag) Pd-Fe<sub>3</sub>O<sub>4</sub> nanocomposites as novel catalysts for methane partial oxidation at low temperature. *Nanomaterials* 10 (5), 988. <https://doi.org/10.3390/nano10050988>.
- Millange, F., Serre, C., Férey, G., 2002. Synthesis, structure determination and properties of MIL-53as and MIL-53ht: the first Cr iii hybrid inorganic–organic microporous solids: Cr<sup>iii</sup>(OH)<sub>2</sub>{O<sub>2</sub>C–C<sub>6</sub>H<sub>4</sub>–CO<sub>2</sub>}<sub>2</sub>{HO<sub>2</sub>C–C<sub>6</sub>H<sub>4</sub>–CO<sub>2</sub>H}<sub>x</sub>. *Chem. Commun.* 8, 822–823. <https://doi.org/10.1039/B201381A>.
- Nguyen, D.T.C., et al., 2019. Metal-organic framework MIL-53 (Fe) as an adsorbent for ibuprofen drug removal from aqueous solutions: response surface modeling and optimization. *J. Chem.* 2019, 1–11. <https://doi.org/10.1155/2019/5602957>.
- Nie, M., et al., 2016. Investigation of the AuPdPt-WC/C electrocatalyst for hydrogen evolution reaction. *J. Electrochem. Soc.* 163 (7), H485. <https://doi.org/10.1149/2.0201607jes>.
- Nie, M., et al., 2020. Novel Pd/MOF electrocatalyst for hydrogen evolution reaction. *Mater. Chem. Phys.* 254, 123481 <https://doi.org/10.1016/j.matchemphys.2020.123481>.
- Nivetha, R., et al., 2020. Highly porous MIL-100 (Fe) for the hydrogen evolution reaction (HER) in acidic and basic media. *ACS Omega* 5 (30), 18941–18949. <https://doi.org/10.1021/acsomega.0c02171>.
- Qi, Q., Shao, D., Zhou, Y., Wang, Q., Yu, X.-Y., 2023. Plasma-induced implanting of active species in metal–organic frameworks for efficient hydrogen evolution reaction. *J. Mater. Chem. A* 11 (29), 15663–15669. <https://doi.org/10.1039/D3TA02610H>.
- Z. Qian, Y. Pei, H. Zareipour, and N. Chen, “A review and discussion of decomposition-based hybrid models for wind energy forecasting applications,” *Applied Energy*, vol. 235. Elsevier Ltd, pp. 939–953, Feb. 01, 2019. doi: 10.1016/j.apenergy.2018.10.080.
- Radwan, A., Jin, H., He, D., Mu, S., 2021. Design engineering, synthesis protocols, and energy applications of MOF-derived electrocatalysts. *Nano-Micro Lett.* 13, 1–32. <https://doi.org/10.1007/s40820-021-00656-w>.
- Tan, Y., Wei, Y., Liang, K., Wang, L., Zhang, S., 2021. Facile in-situ deposition of Pt nanoparticles on nano-pore stainless steel composite electrodes for high active hydrogen evolution reaction. *Int. J. Hydrogen Energy* 46 (52), 26340–26346. <https://doi.org/10.1016/j.ijhydene.2021.05.130>.
- Tang, Z., Liao, L., Zheng, Y., Kang, J., Chen, Y., 2012. Temperature effect on hydrogen evolution reaction at Au electrode. *Chin. J. Chem. Phys.* 25 (4), 469. <https://doi.org/10.1088/1674-0068/25/04/469-474>.
- Tu, M., et al., 2021. Direct X-ray and electron-beam lithography of halogenated zeolitic imidazolate frameworks. *Nat. Mater.* 20 (1), 93–99. <https://doi.org/10.1038/s41563-020-00827-x>.
- Wang, H.-F., Chen, L., Pang, H., Kaskel, S., Xu, Q., 2020. MOF-derived electrocatalysts for oxygen reduction, oxygen evolution and hydrogen evolution reactions. *Chem. Soc. Rev.* 49 (5), 1414–1448. <https://doi.org/10.1039/C9CS00906J>.
- Wang, J., Shao, H., Ren, S., Hu, A., Li, M., 2021. Fabrication of porous Ni-Co catalytic electrode with high performance in hydrogen evolution reaction. *Appl. Surf. Sci.* 539, 148045 <https://doi.org/10.1016/j.apsusc.2020.148045>.
- Wu, L., et al., 2020. Electrochemical performance of porous Ni-alloy electrodes for hydrogen evolution reaction from seawater electrolysis. *RSC Adv.* 10 (73), 44933–44945. <https://doi.org/10.1039/D0RA04320F>.
- Wu, K., et al., 2022. Pyrazine functionalization to boost the antenna effect in rare-earth metal–organic frameworks for tetracycline detection. *Inorg. Chem. Front.* 9 (8), 1714–1721. <https://doi.org/10.1039/D2QI00214K>.
- Xiao, P., et al., 2014. Molybdenum phosphide as an efficient electrocatalyst for the hydrogen evolution reaction. *Energ. Environ. Sci.* 7 (8), 2624–2629. <https://doi.org/10.1039/C4EE00957F>.
- Xu, C., et al., 2022. Synergistically coupling of Ni<sub>3</sub>Mo<sub>3</sub>C/Mo<sub>2</sub>C/Ti<sub>3</sub>C<sub>2</sub>Tx MXene/N-doped carbon electrocatalyst towards enhanced hydrogen evolution activity. *J. Alloy. Compd.* 920, 165826 <https://doi.org/10.1016/j.jallcom.2022.165826>.
- Xu, Y., Huang, K., Zhu, Z., Xia, T., 2019. Effect of glassy carbon, gold, and nickel electrodes on nickel electrocrystallization in an industrial electrolyte. *Surf. Coat. Technol.* 370, 1–10. <https://doi.org/10.1016/j.surfcoat.2019.04.072>.
- Xue, Z., et al., 2019. Missing-linker metal-organic frameworks for oxygen evolution reaction. *Nat. Commun.* 10 (1), 5048. <https://doi.org/10.1038/s41467-019-13051-2>.
- Yalew, S.G., et al., 2020. Impacts of climate change on energy systems in global and regional scenarios. *Nat. Energy* 5 (10), 794–802. <https://doi.org/10.1038/s41560-020-0664-z>.
- Yan, B., Zhang, L., Tang, Z., Al-Mamun, M., Zhao, H., Su, X., 2017. Palladium-decorated hierarchical titania constructed from the metal-organic frameworks NH<sub>2</sub>-MIL-125 (Ti) as a robust photocatalyst for hydrogen evolution. *Appl. Catal. B: Environ.* 218, 743–750. <https://doi.org/10.1016/j.apcatb.2017.07.020>.
- Yin, K., Cheng, Y., Jiang, B., Liao, F., Shao, M., 2018. Palladium–silicon nanocomposites as a stable electrocatalyst for hydrogen evolution. *J. Colloid Interface Sci.* 522, 242–248. <https://doi.org/10.1016/j.jcis.2018.03.045>.
- Yu, J., et al., 2020. One-step synthesis of Mn-doped MIL-53 (Fe) for synergistically enhanced generation of sulfate radicals towards tetracycline degradation. *J. Colloid Interface Sci.* 580, 470–479. <https://doi.org/10.1016/j.jcis.2020.07.045>.
- Zhang, J., et al., 2023. MOF-derived bimetallic NiMo-based sulfide electrocatalysts for efficient hydrogen evolution reaction in alkaline media. *J. Alloy. Compd.* 935, 167974 <https://doi.org/10.1016/j.jallcom.2022.167974>.
- Zhou, H., et al., 2018. Mesoporous-silica induced doped carbon nanotube growth from metal–organic frameworks. *Nanoscale* 10 (13), 6147–6154. <https://doi.org/10.1039/C8NR00137E>.